Title

Multi-parametric hyperpolarized 13C/1H imaging reveals Warburg-related metabolic dysfunction and associated regional heterogeneity in high-grade human gliomas

Authors

Autry, Adam W

Vaziri, Sana

LaFontaine, Marisa

et al.

Publication Date

2023

DOI

10.1016/j.nicl.2023.103501

Peer reviewed

NeuroImage: Clinical 39 (2023) 103501

Contents lists available at ScienceDirect

NeuroImage: Clinical

journal homepage: www.elsevier.com/locate/ynicl

Multi-parametric hyperpolarized $^{13}C/^{1}H$ imaging reveals Warburg-related metabolic dysfunction and associated regional heterogeneity in high-grade human gliomas

Adam W. Autry [a], Sana Vaziri [a], Marisa LaFontaine [a], Jeremy W. Gordon [a], Hsin-Yu Chen [a], Yaewon Kim [a], Javier E. Villanueva-Meyer [a,b], Annette Molinaro [c,b], Jennifer L. Clarke [b,d], Nancy Ann Oberheim Bush [b,d], Duan Xu [a], Janine M. Lupo [a], Peder E.Z. Larson [a], Daniel B. Vigneron [a,e], Susan M. Chang [b], Yan Li [a,*]

[a] Department of Radiology and Biomedical Imaging, University of California, San Francisco, USA
[b] Department of Neurological Surgery, University of California, San Francisco, USA
[c] Department of Epidemiology and Biostatistics, University of California, San Francisco, USA
[d] Department of Neurology, University of California, San Francisco, USA
[e] Department of Bioengineering and Therapeutic Science, University of California, San Francisco, USA

ARTICLE INFO

Keywords:
GBM
Hyperpolarized carbon-13
Metabolism
Treatment effects
IDH

ABSTRACT

Background: Dynamic hyperpolarized (HP)-^{13}C MRI has enabled real-time, non-invasive assessment of Warburg-related metabolic dysregulation in glioma using a [1-^{13}C]pyruvate tracer that undergoes conversion to [1-^{13}C]lactate and [^{13}C]bicarbonate. Using a multi-parametric $^{1}H/HP\text{-}^{13}C$ imaging approach, we investigated dynamic and steady-state metabolism, together with physiological parameters, in high-grade gliomas to characterize active tumor.

Methods: Multi-parametric $^{1}H/HP\text{-}^{13}C$ MRI data were acquired from fifteen patients with progressive/treatment-naïve glioblastoma [prog/TN GBM, IDH-wildtype ($n = 11$)], progressive astrocytoma, IDH-mutant, grade 4 ($G4A^{IDH+}$, $n = 2$) and GBM manifesting treatment effects ($n = 2$). Voxel-wise regional analysis of the cohort with prog/TN GBM assessed imaging heterogeneity across contrast-enhancing/non-enhancing lesions (CEL/NEL) and normal-appearing white matter (NAWM) using a mixed effects model. To enable cross-nucleus parameter association, normalized perfusion, diffusion, and dynamic/steady-state (HP-^{13}C/spectroscopic) metabolic data were collectively examined at the ^{13}C resolution. Prog/TN GBM were similarly compared against progressive $G4A^{IDH+}$ and treatment effects.

Results: Regional analysis of Prog/TN GBM metabolism revealed statistically significant heterogeneity in ^{1}H choline-to-*N*-acetylaspartate index $(CNI)_{max}$, [1-^{13}C]lactate, modified [1-^{13}C]lactate-to-[1-^{13}C]pyruvate ratio ($CEL_{val} > NEL_{val} > NAWM_{val}$); [1-$^{13}C$]lactate-to-[$^{13}C$]bicarbonate ratio ($CEL_{val} > NEL_{val}/NAWM_{val}$); and ^{1}H-lactate ($CEL_{val}/NEL_{val} > NAWM_{undetected}$). Significant associations were found between normalized perfusion (cerebral blood volume, *n*CBV; peak height, *n*PH) and levels of [1-^{13}C]pyruvate and [1-^{13}C]lactate, as well as between CNI_{max} and levels of [1-^{13}C]pyruvate, [1-^{13}C]lactate and modified ratio. GBM, by comparison to $G4A^{IDH+}$, displayed lower perfusion %-recovery and modeled rate constants for [1-^{13}C]pyruvate-to-[1-^{13}C]lactate conversion (k_{PL}), and higher ^{1}H-lactate and [1-^{13}C]pyruvate levels, while having higher *n*CBV, %-recovery, k_{PL}, [1-^{13}C]pyruvate-to-[1-^{13}C]lactate and modified ratios relative to treatment effects.

Conclusions: GBM consistently displayed aberrant, Warburg-related metabolism and regional heterogeneity detectable by novel $HP\text{-}^{13}C/^{1}H$ imaging techniques.

Abbreviations: HGG, high-grade glioma; HP-^{13}C, hyperpolarized carbon-13; mRANO, modified Response Assessment in Neurooncology; MCTs, monocarboxylate transporters; prog/TN, progressive/treatment-naïve; CNI, choline-to-N-acetylaspartate index; EPI, echo-planar imaging; EPA, electron paramagnetic agent.

* Corresponding author at: Department of Radiology and Biomedical Imaging, University of California, 185 Berry Street, Ste. 350, San Francisco, CA 94107, USA.
E-mail address: yan.li@ucsf.edu (Y. Li).

https://doi.org/10.1016/j.nicl.2023.103501
Received 4 May 2023; Received in revised form 29 July 2023; Accepted 16 August 2023
Available online 18 August 2023

1. Introduction

Following extensive development, hyperpolarized carbon-13 (HP-^{13}C) MRI is now being applied to characterize human brain metabolism (Grist et al., 2019; Lee et al., 2020) and its Warburg-related dysregulation (Warburg, 1956) associated with gliomas (Park et al., 2018; Miloushev et al., 2018; Autry et al., 2020, 2021; Chen et al., 2021). This emerging imaging technology relies on an exogenous [1-^{13}C]pyruvate tracer whose ^{13}C label undergoes dynamic nuclear polarization (DNP) to transiently enhance MR signal by approximately 50,000 fold (Ardenkjaer-Larsen et al., 2003). Shortly after the intravenous injection of HP [1-^{13}C]pyruvate in patients, dynamic HP-^{13}C imaging captures the real-time perfusion and subsequent enzymatic conversion of the metabolic substrate over a 60-s timescale. Within the brain, conversion to either [1-^{13}C]lactate via cytosolic lactate dehydrogenase (LDH) or [^{13}C]bicarbonate via mitochondrial pyruvate dehydrogenase (PDH) and carbonic anhydrase (CA) reflects the relative glycolytic versus oxidative character of these respective canonical pathways (Lunt and Vander Haden, 2011; Saraste, 1999).

With Warburg effects being a hallmark of tumor metabolism (Agnihotri and Zadeh, 2016), several translational investigations have sought to evaluate the potential clinical value of *in vivo* HP-^{13}C imaging. In the first HP-^{13}C feasibility study performed on patients with glioma, spectroscopic data demonstrated the rapid uptake of [1-^{13}C]pyruvate through the blood–brain barrier (BBB) and dynamic metabolism in the brain (Park et al. 2018). Further investigation of serial HP-^{13}C imaging provided evidence of aberrant metabolism in progressive contrast-enhancing glioblastoma (GBM) as well as non-enhancing lower-grade glioma, based on the regional kinetic modeling of [1-^{13}C]pyruvate-to-[1-^{13}C]lactate conversion (Autry et al., 2020). Besides excess [1-^{13}C]lactate production, these data supported reduced levels of [^{13}C]bicarbonate in GBM, consistent with Warburg modification to mitochondrial oxidative phosphorylation (Saraste, 1999). More recent HP imaging studies have corroborated such metabolic dysregulation in treatment-naïve patients with newly-diagnosed GBM (Chen et al., 2021; Zaccagna et al., 2022) and demonstrated predictive value for response to therapy in brain metastases of various origins (Lee et al., 2021). From the perspective that alterations to glioma metabolism precede more macroscopic anatomical and physiologic changes, HP data may reveal early markers of tumor evolution and response to therapy that could augment conventional imaging. This is of particular interest given the longstanding diagnostic dilemma facing neuro-oncology in characterizing glioma progression versus treatment-related effects from nonspecific anatomical changes on MRI (Da Cruz et al., 2011).

While HP-^{13}C methods provide a readout of short-lived dynamic metabolism in the brain, ^{1}H spectroscopy has been shown to detect various aspects of steady-state metabolism, which are also relevant to evaluating glycolytic dysfunction and molecular alterations of glioma. The use of steady-state magnetic resonance spectroscopic imaging (^{1}H-MRSI) has enabled the detection of excess lactate that is formed in lesions through aerobic glycolysis and readily excreted by astrocyte monocarboxylate transporters (MCTs) (Saraswathy et al., 2009; Miranda-Goncalves et al., 2013). Moreover, the MRSI-based choline-to-*N*-acetylaspartate (NAA) index (CNI) has been used as a composite measure of aberrant metabolism, based on excess choline-containing species associated with tumor proliferation, and reduced NAA levels resulting from compromised neuronal function (McKnight et al., 2001). Both steady-state lactate and CNI are well established as parameters holding prognostic value (Saraswathy et al., 2009).

By using a multi-parametric ^{1}H/HP-^{13}C imaging strategy to evaluate dynamic and steady-state metabolism, in conjunction with physiologic features, this study aimed to improve the characterization of active disease in patients with high-grade glioma (HGG). As a central focus of the investigation, we assessed the presence of aberrant metabolism in GBM and associated heterogeneity across anatomical lesions through voxel-wise regional analysis of the data. Potential relationships between HP-^{13}C and ^{1}H imaging parameters were also evaluated to determine their relative association. Our primary hypothesis was that progressive GBM would express region-dependent, heterogeneous metabolic dysregulation that could be detected via HP-^{13}C techniques and thusly provide novel tumor contrast on imaging. Secondary analyses concerned the potential to differentiate between HGG subtypes and active disease versus treatment-related effects. Given the tremendous technical and logistical demands of HP-^{13}C experiments, this study is distinguished for having the largest collection of HP data from patients with progressive gliomas and represents the cumulative advancement of ^{13}C-based methodology.

2. Material and methods

2.1. Patient population

Fifteen patients (6/9 female/male; 51.7 ± 11.2 years, mean ± SD) with newly diagnosed HGG (treatment-naïve; TN, $n = 2$) or suspected progression were recruited, and all the subjects provided written informed consent in accordance with the University of California San Francisco IRB procedures. Tumor classification and grading were performed according to CNS WHO 2021 guidelines (Louis et al., 2021) using surgically-derived tissue from 2 astrocytoma, isocitrate dehydrogenase (IDH)-mutant, grade 4 (G4A^{IDH+}) and 13 GBM, IDH-wildtype. Additional molecular information was obtained for each patient from a comprehensive genetic panel that evaluated known pathologic mutations in glioma (UCSF500 Cancer Gene Panel Test, UCSF). Among those with suspected tumor progression, the determination of progression ($n = 2$/9 G4A^{IDH+}/GBM) versus treatment effects ($n = 2$ GBM) was made either on the basis of surgical pathology or modified Response Assessment in Neurooncology (*m*RANO) imaging criteria (Ellingson et al., 2017) together with serial imaging. Inclusion criteria required adults with Karnofsky performance scores ≥ 70; within-tolerance creatinine clearance for receiving a gadolinium-based contrast agent; and normal cardiac function, as measured by EKG. Additionally, prior treatment with anti-angiogenic agent bevacizumab was an exclusionary factor because of the known impact to HP kinetics (Autry et al. 2020). A total of 19 multi-parametric HP-^{13}C/^{1}H MR examinations were performed, with 4 subjects having undergone a second MRI for another suspected progression.

2.2. HP-^{13}C/^{1}H MR examination

All MR imaging data was acquired on a 3 Tesla MR750 scanner (GE Healthcare Technologies, Waukisha, WI) using either a dual-tuned 8/24-channel ^{1}H/^{13}C headcoil (14/19 scans, Rapid Biomedical, Rimpar, Germany) or a combination of the 8-channel bilateral ^{13}C paddle coils (4/19 scans) or ^{13}C volume headcoil (1/19 scans) for carbon imaging (Autry et al., 2020) and separate 32-channel ^{1}H headcoil for proton imaging. The dual-tuned coil enabled a continuous exam with integrated ^{1}H/HP-^{13}C imaging, whereas other hardware configurations necessitated the swapping of receiver coils in between ^{13}C and ^{1}H series.

Preparation of the HP agent entailed compounding and polarization procedures. Pharmacy kits containing a mixture of 1.432 g [1-^{13}C]pyruvic acid (MilliporeSigma, Miamisburg, OH) and 28 mg electron paramagnetic agent (EPA: AH111501; GE Healthcare, Oslo, Norway) were prepared under ISO 5 environment. During polarization, the sample was maintained at 5 Tesla and 0.8 Kelvin for ≥ 2.5 hr in a SPINlab (General Electric, Niskayuna, NY) while being irradiated at microwave frequencies near 140 GHz. Upon initiating experiments, polarized samples were rapidly heated for dissolution in sterile water; passed through an EPA filter; and neutralized and diluted using a sodium hydroxide tris(hydroxymethyl) aminomethane/ethylenediaminetetraacetic acid buffer solution. An integrated quality control (QC) system measured the resulting pH, temperature, residual EPA concentration, volume, [1-^{13}C]pyruvate concentration, and polarization level. Before

collection in a MEDRAD syringe (Bayer HealthCare, Pittsburgh, PA), the sample underwent terminal sterilization in a filter (0.2 μm; ZenPure, Manassas, VA).

Contingent on acceptable QC parameters (polarization ≥ 15%; pyruvate concentration, 220–280 mM; EPA concentration ≤ 3.0 μM; pH, 5.0–9.0; temperature, 25–37 °C; volume > 38 mL; and bubble point test on sterilizing filter passed at 50 psi), a pharmacist released the HP [1-^{13}C]pyruvate tracer for injection with a dosage of 0.43 mL/kg and 5 mL/s delivery rate, followed by a 20 mL sterile saline flush. HP data were acquired using a dynamic 2D multi-slice echo-planar imaging (EPI) sequence (TR/TE = 62.5 ms/21.7 ms, 24 × 24 cm^2 FOV, 8 slices, 20 timepoints, 3 s temporal resolution, 60 s total acquisition time) with 15 × 15 × 15 mm^3 spatial resolution, which sequentially excited [1-^{13}C] pyruvate (Pyr), [1-^{13}C]lactate (Lac) and [^{13}C]bicarbonate (Bic) resonances according to the flip angle scheme [α_{pyr},α_{lac},α_{bic}] = [20°,30°,30°] (Gordon et al., 2019). The [1-^{13}C]pyruvate center frequency was referenced using either a coil-embedded 1 mL 8 M ^{13}C-urea phantom or water with an empirically-determined ^{1}H–^{13}C gyromagnetic conversion ratio (0.251491899). A 5 s acquisition delay post injection accommodated the systemic circulation of HP [1-^{13}C]pyruvate. Following HP-^{13}C injection, patient vital signs (blood pressure, pulse) were monitored for safety by the attending nurse.

The ^{1}H MRI brain tumor protocol included T_2-weighted fluid-attenuated inversion recovery (FLAIR); pre/post-contrast T_1-weighted inversion recovery spoiled gradient echo (IR-SPGR); 24-direction diffusion (TR/TE = 7500/62 ms, matrix = 128 × 128, voxel size = 1.9 × 1.9 × 2 mm^3, b = 1000 s/mm^2)(1/19 cases had clinical diffusion acquired); and dynamic susceptibility contrast-enhanced (DSC) perfusion images (TR/TE = 1250–1500/ 35–54 ms, 30–35^0 flip angle, 128 × 128 matrix, 3–5 mm slice thickness, 7–15 slices; 3 mL/s bolus injection of 0.1 mmol/kg gadolinium diethyltriamine penta-acetic acid; Lupo et al., 2007). In earlier exams where dual-tuned hardware was unavailable, T_2-weighted fast spin-echo (FSE) images were acquired for anatomical reference using the ^{1}H body coil. ^{1}H lactate-edited MR spectroscopic imaging (MRSI; TR/TE = 1300/144 ms, matrix size = 18 × 18 × 16, nominal voxel size = 1 × 1 × 1 cm^3, flyback echo-planar readout; T_{acq}=~10 min; Park et al., 2011) was also acquired to provide a readout of steady-state metabolism in the brain in all but one exam.

2.3. HP-^{13}C/^{1}H data processing

EPI data were prewhitened via Cholesky decomposition (Nash, 1990) of the noise covariance matrix, channel-combined using complex weights from the fully sampled [1-^{13}C]pyruvate signal (Zhu et al., 2019), phased and denoised (Kim et al., 2021). Combined kinetic modeling of rate constants for pyruvate-to-lactate (k_{PL}) and pyruvate-to-bicarbonate (k_{PB}) conversion was performed on dynamic data using an inputless model (Larson et al., 2018). Rate constant errors were estimated from nonlinear least squares residuals from fitted traces and thresholded < 25%. Summing the data over time provided area-under-the-curve (AUC) metabolite images, which were normalized by flip angles and thresholded at a signal-to-noise ratio (SNR) > 5 to obtain *n*Lac-to-*n*Pyr, *n*Lac-to-*n*Bic, and *n*Bic-to-*n*Pyr ratios. Because pyruvate forms the dominant contribution to HP signal in the brain, with only a small fraction undergoing conversion, there is a substantial portion that represents non-metabolically-active vascular substrate or excess accumulation. This has a confounding effect on the evaluation of *n*Lac-to-*n*Pyr ratios and k_{PL} modeling, which depend on the vascular content of a given region. To account for such vascular substrate, we proposed a modified *n*Lac-to-*n*Pyr ratio that normalizes the total pyruvate signal with respect to unconverted tracer. By subtracting metabolite signal representing pyruvate that has undergone conversion, we tentatively expressed "vascular pyruvate" using the proportion of $nPyr - (nLac + nBic)$ relative to the total carbon signal, $nPyr + nLac + nBic$:

$$nPyr\left[\frac{nPyr-(nLac+nBic)}{nPyr+nLac+nBic}\right]$$

To obtain a corrected measure of pyruvate, the "vascular pyruvate" was subtracted from the total pyruvate:

$$nPyr - nPyr\left[\frac{nPyr-(nLac+nBic)}{nPyr+nLac+nBic}\right]$$

Substituting this expression for corrected pyruvate into the standard lactate-to-pyruvate ratio and rearranging yields the modified ratio:

$$\text{Modified ratio} = \frac{n\text{Lac}}{n\text{Pyr}\left[1-\frac{n\text{Pyr}-(n\text{Lac}+n\text{Bic})}{n\text{Pyr}+n\text{Lac}+n\text{Bic}}\right]}$$

Percentile maps ([1-^{13}C]Pyr$_{pct}$, [1-^{13}C]Lac$_{pct}$, [^{13}C]Bic$_{pct}$) of AUC metabolite images were calculated over the entire brain to report on individual resonances. Rate constant maps and AUC images were linearly interpolated by a factor of 2 in-plane to improve regional comparison with proton-based parameters.

White matter was segmented on pre-contrast T_1-weighted images using the FSL FAST algorithm (Zhang et al., 2001), then refined by removing cortical and deep grey structures of the AAL3 atlas (Rolls et al., 2020). The T_2-hyperintense FLAIR lesion (T2L) and contrast-enhancing lesion (CEL) were semi-automatically segmented with 3D Slicer software (Menze et al., 2015). A normal-appearing white matter (NAWM) mask was generated by subtracting the T2L from segmented white matter; and the non-enhancing lesion (NEL) was defined as T2L minus CEL. For the 5 exams where data were acquired with separate ^{1}H and ^{13}C receiver coils, ^{1}H images and ROIs were aligned to FSE images (Autry et al., 2020) obtained during the ^{13}C exam using FSL FLIRT (Jenkinson and Smith, 2001). Interpolated ^{13}C data voxels were exclusively categorized as NAWM, NEL or CEL based on the percent volume occupied by associated ^{1}H ROIs: NAWM (≥60%), NEL (≥60%), or CEL (≥20%).

^{1}H imaging data were processed as described previously to generate established imaging parameters for evaluating patients with glioma, including apparent diffusion coefficients (ADC; Basser and Pierpaoli, 1996) from diffusion imaging; relative cerebral blood volume (rCBV), peak height (PH) and percent recovery (REC) from DSC perfusion (Lupo et al., 2007). The 3D MRSI data were reconstructed using in-house software that applied time domain apodization, Fourier transformation, frequency and phase correction, baseline removal, and peak estimation for individual metabolite amplitudes (Nelson, 2001; Crane et al., 2013); lactate intensity was estimated from the difference spectra of editing pulse ON/OFF cycles (Park et al., 2011). Calculation of CNI was performed through an automatic, iterative procedure that generated z-scores based on the abnormality presented by relative levels of total choline and NAA over the entire spectral array (McKnight et al., 2001). Diffusion and perfusion parameters were normalized (*n*[parameter]) by the median values within normal-appearing white matter (NAWM), while ^{1}H-lactate was normalized by median NAA in NAWM.

2.4. Statistical analysis

To evaluate multi-parametric imaging in the same space, masks at the interpolated ^{13}C resolution (7.5 × 7.5 mm^2 in-plane, 2x interpolation; 15-mm slice thickness) were iteratively applied to ^{1}H data on a voxel-wise basis. Median (med), mean, maximum (max) and 10th/90th percentile values of ^{1}H data were calculated within each ^{13}C-resolution ROI (CEL, NEL, NAWM) voxel. Multi-parametric data were then collectively compared across ROIs and patient groups using a random mixed effects model that accounted for repeated ROI sampling within a patient. In the 4 cases where patients were scanned twice, each scan was treated as independent due to the evolved tumor presentation, including the emergence of a new focus, intervening surgery/treatment, and or long inter-scan intervals (see Supplementary Table 1). Associations between ^{1}H and HP-^{13}C parameters were assessed in patients with prog/

TN GBM using a linear mixed effects model, which included the CEL as a fixed effect, and the patient as a random intercept to account for within-subject correlations; an additional CEL*^{13}C interaction term was also tested. Akaike information criterion (AIC) values were used to compare the fit qualities of the models (with and without interaction), and the model with the lower AIC was chosen. As this was an exploratory analysis, no correction was made for multiple comparisons. Analyses were performed in R v4.0.2.

3. Results

3.1. Patient characterization

Table 1 contains a clinical summary of the fifteen patients recruited to the study, with 2 subjects being treatment-naïve prior to imaging and the remainder having received a variety of adjuvant therapies alongside standard-of-care treatment with external beam radiotherapy (RT) and temozolomide (TMZ). Among those with suspected tumor progression, confirmation of progression at each timepoint was determined either by a subsequent surgery (n = 1/8 instances, G4A^{IDH+}/GBM) or *m*RANO (Ellingson et al., 2017) imaging criteria (n = 2/5 scans, G4A^{IDH+}/GBM); whereas treatment effects were evaluated either on the basis of surgical pathology (n = 0/1 instance, G4A^{IDH+}/GBM) or serial imaging (n = 0/2 scans, G4A^{IDH+}/GBM). Such classification provided three distinct patient populations for analysis: prog/TN GBM (n = 11; 9/2 prog/TN), progressive G4A^{IDH+} (n = 2), and GBM exhibiting treatment effects (n = 2).

Fig. 1 demonstrates the molecular diversity of patient lesions from pathologic mutations identified by the UCSF500 genetic panel. Segmented NEL and CEL volumes are provided for each scan in Supplementary Table 1, with mean volumes of GBM (CEL/NEL = 10.8/57.6 cm^3) and astrocytoma, IDH-mutant, grade 4 (CEL/NEL = 1.7/28.0) revealing that IDH-mutant tumors were typically smaller in size and sometimes almost entirely non-enhancing. This table also includes the inter-scan intervals and treatment for the 4 patients who were scanned twice.

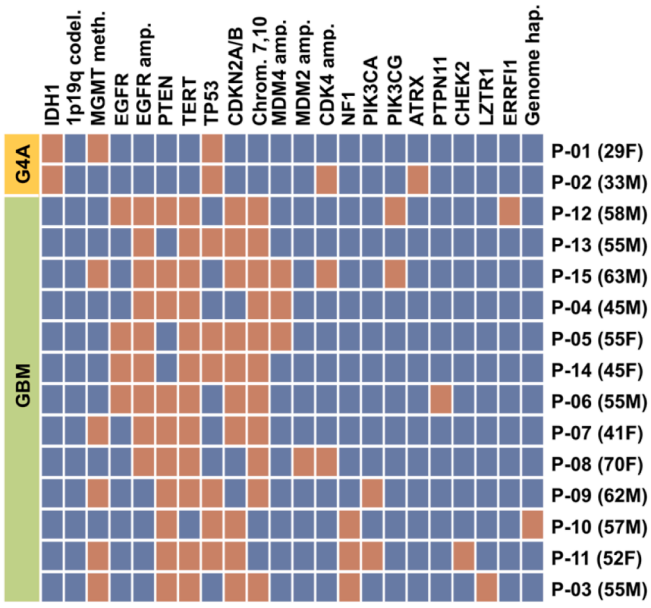

Fig. 1. Molecular tumor characterization. Pathological mutations identified in patients with GBM and G4A^{IDH+} based on the UCSF500 genetic panel.

3.2. Regional analysis of progressive/TN GBM

Two patients with characteristic multi-parametric ^{1}H/HP-^{13}C profiles of TN GBM are presented in Fig. 2. While both exhibited clear elevations in AUC HP [1-^{13}C]Pyr and HP [1-^{13}C]Lac within the lesion, a slightly different emphasis is placed on their vascular versus metabolic characteristics, based on the particular circumstances of data collection and the unique examples they offer. The first patient displayed classic angiogenic abnormalities in the CEL on the basis of elevated rCBV from DSC perfusion and AUC HP [1-^{13}C]Pyr, which, unlike Gd chelates, is actively transported across the plasma membrane as a small molecule[1] (Fig. 2**A**). The elevations in AUC HP [1-^{13}C]Pyr generally mirrored those

Table 1
HGG patient population. Clinical summary of patient characteristics, including diagnosis, progression status and treatment history. Follow-up intervals are indicated for patients with progression determined by *m*RANO criteria. NA, not applicable; IDH, isocitrate dehydrogenase; *m*RANO, modified Response Assessment in Neuro-oncology; Tx, treatment; Sx, surgery; RT, radiotherapy; TMZ, temozolomide; CCNU, lomustine.

Patient ID	Diagnosis	Disease status	Age (yr), Sex	Progression vs treatment effect status at time of scan	Method of assessing progression/ Tx effects (follow-up intervals in months)	Treatment history
P-01	astrocytoma, IDH-mutant, grade 4	recurrent	29F	progression	*m*RANO (2, 1)	Sx, RT/TMZ
P-02	astrocytoma, IDH-mutant, grade 4	recurrent	33 M	progression	surgery	Sx, RT/TMZ, Optune
P-03	GBM, IDH-wildtype	recurrent	55 M	progression	*m*RANO (2)	Sx, RT/TMZ, CCNU, trametinib, everolimus, abemaciclib
P-04	GBM, IDH-wildtype	recurrent	45 M	progression	surgery, *m*RANO (2.5)	Sx, RT/TMZ, nivolumab, poliovirus infusion
P-05	GBM, IDH-wildtype	recurrent	55F	progression	surgery, surgery	Sx, RT/TMZ
P-06	GBM, IDH-wildtype	recurrent	55 M	progression	surgery	Sx, RT/TMZ
P-07	GBM, IDH-wildtype	recurrent	41F	progression	surgery	Sx, RT/TMZ, olaparib, afatinib
P-08	GBM, IDH-wildtype	recurrent	70F	progression	*m*RANO (1)	Sx, RT/TMZ, CCNU, afatinib, abemaciclib
P-09	GBM, IDH-wildtype	recurrent	62 M	progression	*m*RANO (3)	Sx, RT/TMZ, Newcastle Disease virus + hyperthermia, olaparib, everolimus
P-10	GBM, IDH-wildtype	recurrent	57 M	progression	*m*RANO (0.5)	Sx, RT/TMZ
P-11	GBM, IDH-wildtype	recurrent	52F	progression	surgery	Sx, RT/TMZ
P-12	GBM, IDH-wildtype	newly diagnosed	58 M	NA	surgery	*treatment-naive*
P-13	GBM, IDH-wildtype	newly diagnosed	55 M	NA	surgery	*treatment-naive*
P-14	GBM, IDH-wildtype	recurrent	45F	treatment effects	surgery	Sx, RT/TMZ, pamiparib (BGB-290)
P-15	GBM, IDH-wildtype	recurrent	63 M	treatment effects	serial imaging (2, 2)	Sx, RT/TMZ, Optune

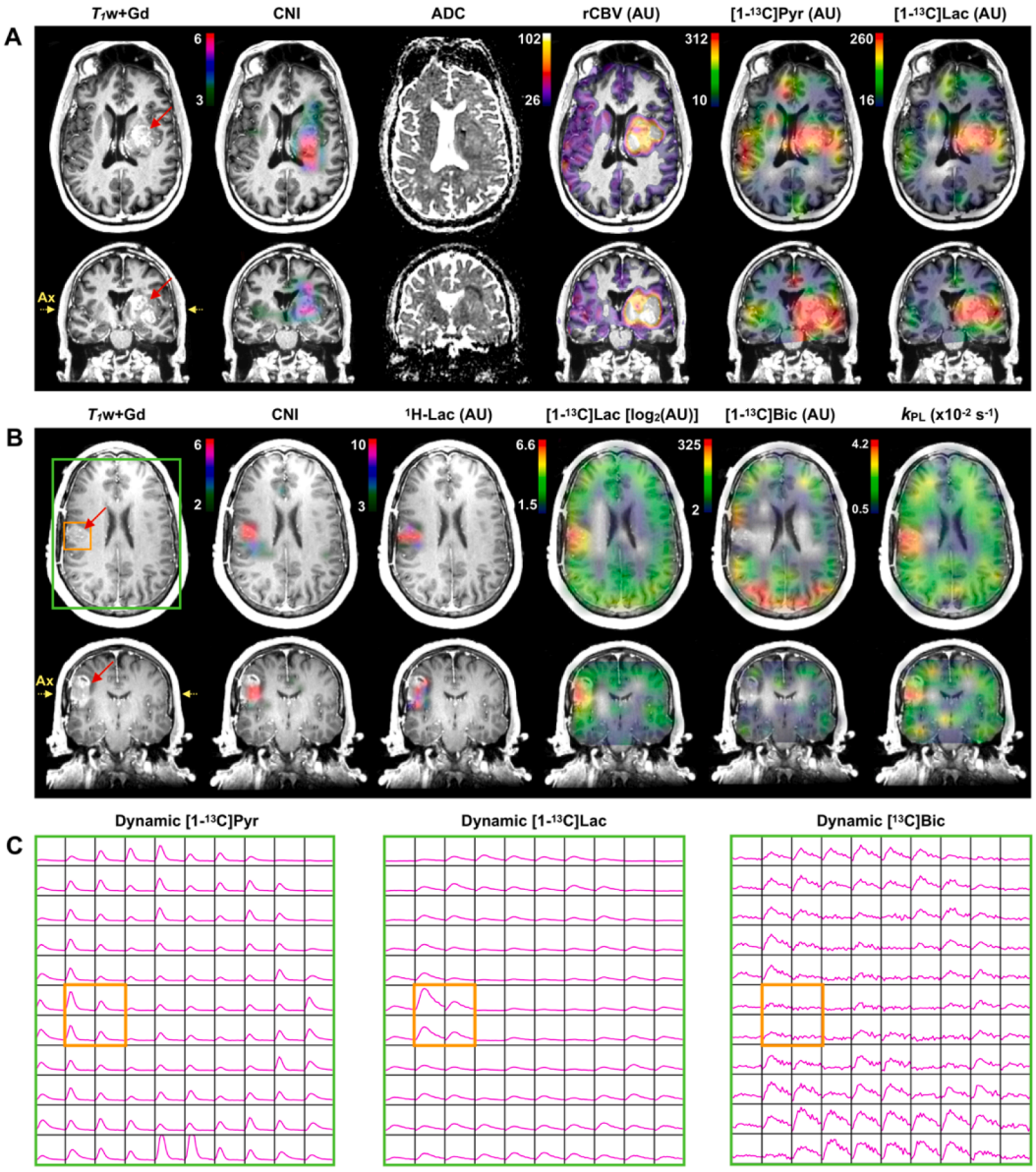

Fig. 2. ^{1}H/HP-^{13}C MRI of treatment-naïve GBM. Multi-parametric ^{1}H/HP-^{13}C MRI data from two patients with TN GBM (*red arrows*) are overlaid on T_1-weighted post-contrast(Gd) images. In the first case, the steady-state metabolic abnormality defined by ^{1}H spectroscopic CNI is co-localized with the rCBV and HP [1-^{13}C]Pyr perfusion abnormalities, as well as excess levels of HP [1-^{13}C]Lac; the diffusion ADC map displays both hyper- and hypo-intense regions (A). The second case clearly demonstrates upregulated Warburg metabolism within the lesion through excess production of lactate (steady-state ^{1}H-Lac; HP [1-^{13}C]Lac) and concomitant reduction in HP [^{13}C]Bic; the k_{PL} map describing [1-^{13}C]Pyr-to-[1-^{13}C]Lac conversion also shows lesion contrast (B). Yellow arrows demark axial (Ax) slice locations on the coronal plane. Dynamic HP metabolite traces corresponding to the outlined lesion (*orange box*) in *B* depict aberrant metabolism over the 60-s acquisition (C). (For interpretation of the references to colour in this figure legend, the reader is referred to the web version of this article.)

of rCBV, with slight deviations being attributable to differences in spatial resolution, ^{1}H/^{13}C coil profiles and tracer size. In this case, the metabolic abnormality is demarked by elevations in AUC HP [1-^{13}C]Lac from HP-^{13}C imaging and CNI from ^{1}H MRSI (^{1}H-lactate-edited data were not collected). This was the only instance where HP data were acquired with a ^{13}C volume receiver coil, allowing AUC metabolite maps to be viewed without the sensitivity bias of a multi-channel coil (ratio/kinetic maps are unaffected). The second patient highlights the elevated AUC HP [1-^{13}C]Lac and concomitant reduction in AUC HP [^{13}C]Bic in the CEL, indicative of altered dynamic metabolism (Fig. 2**B; see Supplementary** Fig. 1 **for HP-^{13}C metabolite SNR**). Whereas HP [1-^{13}C]Lac was observed throughout the brain, spectroscopic measurement of steady-state ^{1}H-Lac demonstrated localization in the lesion. Elevations in maps of CNI and kinetic rate constant k_{PL} helped delineate the most proliferative and glycolytically active portions of the lesion, respectively. Although k_{PL} was not consistently elevated across the GBM population, this patient showed perhaps less vascular influence from HP [1-^{13}C]Pyr on kinetic modeling (modeling of k_{PB} was generally compromised in the lesion due to low [^{13}C]Bic SNR).

As shown in Fig. 3 and Table 2, multi-parametric ^{1}H/HP-^{13}C imaging of patients with prog/TN GBM (n = 11 subjects /13 scans) revealed regional heterogeneity based on the voxel-wise ROI analysis. All of the imaging parameters reporting on diffusion, perfusion, and steady-state/dynamic metabolism displayed statistically significant differences between the CEL and NAWM. When comparing CEL versus NEL, only REC_{med}, $nADC_{med}$, and [^{13}C]Bic/[1-^{13}C]Pyr lacked statistical significance. Importantly, [1-^{13}C]Pyr_{pct} (CEL vs. NEL, CEL vs. NAWM, NEL vs. NAWM: $p < 0.001$, <0.001, <0.001), [1-^{13}C]Lac_{pct} ($p < 0.001$, <0.001,

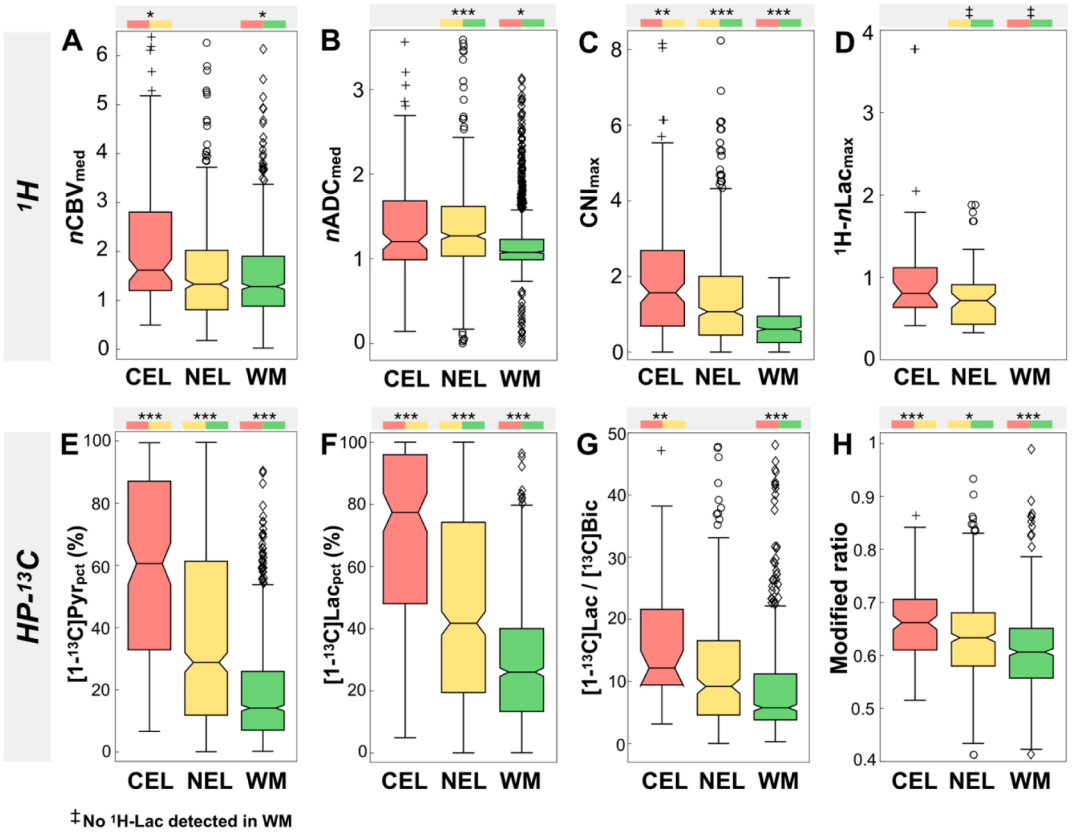

Fig. 3. Regional heterogeneity in prog/TN GBM. Multi-parametric ^{1}H/HP-^{13}C MRI displayed significant regional heterogeneity within prog/TN GBM lesions and relative to NAWM: nCBV$_{med}$ (A), nADC$_{med}$ (B), CNI$_{max}$ (C), ^{1}H-nLac$_{max}$ (D), [1-^{13}C]Pyr$_{pct}$ (E), [1-^{13}C]Lac$_{pct}$ (F), [1-^{13}C]Lac/[^{13}C]Bic (G) and modified ratio (H). Mixed effects model significance: $p \leq 0.001$,***; $p \leq 0.01$,**; $p \leq 0.05$,*. CEL, contrast-enhancing region; NEL, non-enhancing lesion; WM, normal-appearing white matter; ‡, statistical significance could not be tested since no ^{1}H-lacate was detected in WM.

<0.001), modified ratio ($p = 0.014$, <0.001, 0.001), and ^{1}H spectroscopic CNI$_{max}$ ($p < 0.001$, <0.001, 0.002) were significantly different among all 3 analyzed regions.

In HP-^{13}C imaging, the dynamic measures of [1-^{13}C]Pyr perfusion and metabolism were shown to impart lesion contrast. The CEL was distinguished from both the NEL and NAWM by elevations in [1-^{13}C]Pyr$_{pct}$ (CEL vs. NEL, $p < 0.001$; CEL vs. NAWM, $p < 0.001$), [1-^{13}C]Lac$_{pct}$ (CEL vs. NEL, $p < 0.001$; CEL vs. NAWM, $p < 0.001$) and modified ratio (CEL vs. NEL, $p = 0.001$; CEL vs. NAWM, $p < 0.001$); and increased [1-^{13}C]Lac/[^{13}C]Bic (CEL vs. NEL, $p = 0.008$; CEL vs. NAWM, $p < 0.001$) (Fig. 3;Table 2). The NEL was similarly differentiated from NAWM with higher values of [1-^{13}C]Pyr$_{pct}$ ($p < 0.001$), [1-^{13}C]Lac$_{pct}$ ($p < 0.001$) and modified ratio ($p = 0.014$), enabling isolation of the T2L using exclusively HP-^{13}C parameters. Lower values of [^{13}C]Bic/[1-^{13}C]Pyr were also found in the CEL relative to NAWM ($p = 0.023$).

On the other hand, proton-based imaging distinguished the CEL from both the NEL and NAWM on account of elevations in DSC perfusion parameters median nCBV (nCBV$_{med}$) (CEL vs. NEL, $p = 0.012$; CEL vs. NAWM, $p = 0.015$) and nPH$_{med}$ (CEL vs. NEL, $p < 0.001$; CEL vs. NAWM, $p = 0.015$), as well as higher values of ^{1}H spectroscopic parameter CNI$_{max}$ (CEL vs. NEL, $p < 0.001$; CEL vs. NAWM, $p < 0.001$) (Fig. 3; Table 2). CNI$_{max}$ additionally displayed higher values in the NEL versus NAWM ($p = 0.002$), while DSC perfusion parameter REC$_{med}$ was only able to differentiate CEL from NAWM ($p = 0.002$). The anatomic lesions (CEL or NEL) were collectively distinguished from NAWM via increases in nADC$_{med}$ (CEL vs. NAWM, $p < 0.001$; NEL vs. NAWM, $p = 0.041$) and steady-state ^{1}H-nLac from spectroscopy, which was only detected in the CEL + NEL lesion.

The above parameters remained statistically significant when removing the TN cohort (2 patients, 2 scans) from the analysis.

3.3. ^{1}H/HP-^{13}C associations within progressive/TN GBM

Cross-nucleus associations were evaluated among ^{1}H/HP-^{13}C parameters of interest for dynamic/steady-state metabolism and perfusion, based on their statistical relevance from the regional analysis of prog/TN GBM. It was found within GBM lesions (T2L) that: nPH$_{med}$ was associated with [1-^{13}C]Pyr$_{pct}$ ($p < 0.001$) and [1-^{13}C]Lac$_{pct}$ ($p < 0.001$); nCBV$_{med}$ was associated with [1-^{13}C]Pyr$_{pct}$ ($p < 0.001$) and [1-^{13}C]Lac$_{pct}$ ($p < 0.001$); and CNI$_{max}$ was associated with [1-^{13}C]Pyr$_{pct}$ ($p < 0.001$), [1-^{13}C]Lac$_{pct}$ ($p < 0.001$), and modified ratio ($p < 0.001$) (Fig. 4).

3.4. Progressive/TN GBM vs G4A^{IDH+}

When comparing multi-parametric imaging of prog/TN GBM ($n = 11$ subjects /13 scans) with the smaller cohort of progressive G4A^{IDH+} ($n = 2$ subjects /3 scans), statistically significant differences were observed across several parameters in the T2L. These included lower REC$_{med}$ ($p < 0.001$) and higher steady-state ^{1}H-nLac$_{max}$ ($p < 0.001$) from ^{1}H imaging in prog/TN GBM, as well as lower k_{PL} ($p = 0.002$) and higher [1-^{13}C]Pyr$_{pct}$ ($p = 0.006$) from HP-^{13}C data (Fig. 5; Table 2). Figs. 6 and 7 present an example of how elevated perfusion, as measured by [1-^{13}C]Pyr$_{pct}$ and gadolinium-based methods, might artificially lower k_{PL} values in GBM relative to G4A^{IDH+}.

3.5. Progressive/TN GBM vs treatment effects

Imaging differences in prog/TN GBM versus treatment effects were highlighted in both the CEL and overall T2L. As compared to treatment effects, prog/TN GBM displayed greater nCBV$_{med}$ ($p = 0.007$) and

Table 2
^{1}H/HP-^{13}C MRI features of HGGs. Statistically significant multi-parametric ^{1}H/HP-^{13}C features characterizing patients with prog/TN GBM, treatment effects, and G4A^{IDH+}. Voxel-wise analysis was performed for ^{1}H/HP-^{13}C parameters at the interpolated ^{13}C resolution (7.5 × 7.5 mm^2, 2-fold in-plane interpolation; 15-mm slice thickness). Tx effects, treatment-induced effects.

Comparison	^{1}H/^{13}C Parameter	Patients (scans)	Parameter values median (lower, upper quartile)			*p*-value (mixed effects model)		
GBM ROIs			**CEL**	**NEL**	**NAWM**	**CEL vs NEL**	**CEL vs NAWM**	**NEL vs NAWM**
DSC perfusion	nCBV$_{med}$	11(13)	1.63 (1.20, 2.80)	1.33 (0.81, 2.02)	1.29 (0.88, 1.90)	0.012	0.015	NS
	nPH$_{med}$	11(13)	1.73 (1.24, 2.37)	1.29 (0.87, 2.02)	1.42 (0.98, 2.08)	< 0.001	0.049	NS
	REC$_{med}$ (%)	11(13)	88.37 (84.67, 92.79)	88.67 (84.29, 91.74)	90.06 (86.63, 92.76)	NS	0.002	NS
diffusion	nADC$_{med}$	11(13)	1.21 (0.99, 1.68)	1.27 (1.03, 1.62)	1.08 (0.99, 1.23)	NS	0.041	< 0.001
spectroscopy	CNI$_{max}$	11(13)	1.58 (0.70, 2.68)	1.07 (0.45, 2.00)	0.62 (0.26, 0.97)	0.002	< 0.001	< 0.001
	^{1}H-nLac$_{max}$	11(12)	0.81 (0.64, 1.11)	0.72 (0.43, 0.91)	[a]	NS	NS[a]	NS[a]
HP-^{13}C	[1-^{13}C]Pyr$_{pct}$ (%)	11(13)	60.58 (32.88, 87.03)	28.82 (11.87, 61.31)	14.13 (7.05, 25.90)	< 0.001	< 0.001	< 0.001
	[1-^{13}C]Lac$_{pct}$ (%)	11(13)	77.57 (48.10, 95.98)	41.76 (19.49, 74.23)	26.04 (13.40, 40.02)	< 0.001	< 0.001	< 0.001
	[1-^{13}C]Lac/[^{13}C] Bic	11(13)	12.16 (9.44, 21.52)	9.21 (4.61, 16.55)	5.79 (3.81, 11.21)	0.008	< 0.001	NS
	[^{13}C]Bic/[1-^{13}C] Pyr	11(13)	0.0024 (0.0005, 0.0036)	0.0040 (0.0017, 0.0072)	0.0056 (0.0032 0.0086)	NS	0.023	NS
	modified ratio	11(13)	0.66 (0.61, 0.71)	0.63 (0.58, 0.68)	0.61 (0.56, 0.65)	0.001	< 0.001	0.014
GBM vs G4A^{IDH+}			**GBM**	**G4A^{IDH+}**		**GBM vs G4A^{IDH+}**		
T2L	REC$_{med}$ (%)	11(13),2(3)	88.53 (84.48,92.10)	95.40 (93.25,97.71)		< 0.001		
	^{1}H-nLac$_{max}$	11(13),2(3)	0.74 (0.49, 0.95)	0.48 (0.42, 0.58)		< 0.001		
	k_{PL} (s^{-1})	11(13),2(3)	0.020 (0.016, 0.025)	0.027 (0.022, 0.034)		0.002		
	[1-^{13}C]Pyr$_{pct}$ (%)	11(13),2(3)	34.83 (14.53, 69.22)	31.17 (17.56, 43.99)		0.006		
GBM vs Tx effects			**GBM**	**Tx effects**		**GBM vs Tx effects**		
T2L	REC$_{med}$ (%)	11(13),2(3)	88.53 (84.48, 92.10)	84.65 (76.50, 89.61)		0.047		
	k_{PL} (s^{-1})	11(13),2(3)	0.020 (0.016, 0.025)	0.018 (0.014, 0.022)		0.007		
	modified ratio	11(13),2(3)	0.64 (0.59, 0.69)	0.61(0.56, 0.66)		0.018		
CEL	nCBV$_{med}$	11(13),2(3)	1.62 (1.20,2.80)	1.29 (0.95, 2.03)		0.007		
	[1-^{13}C]Lac/[1-^{13}C] Pyr	11(13),2(3)	0.36 (0.27, 0.42)	0.33 (0.27, 0.36)		0.019		

[a] no ^{1}H-nLac detected in NAWM.

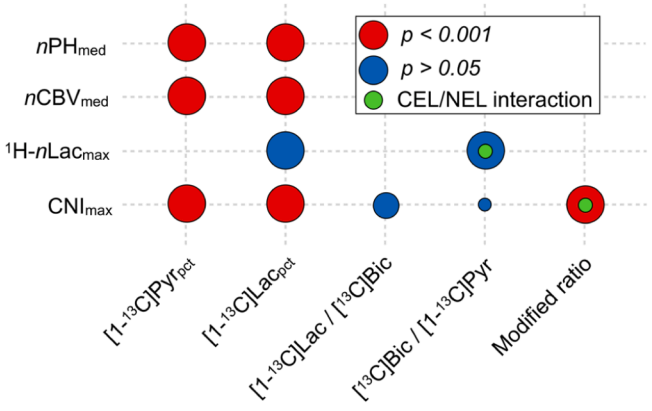

Fig. 4. ^{1}H–^{13}C parameter associations. Associations evaluated between ^{1}H and HP-^{13}C parameters. Statistical significance: $p < 0.001$ (*red*); $p > 0.05$ (*blue*); significant model interaction indicating that the CEL was driving the association (*green*). (For interpretation of the references to colour in this figure legend, the reader is referred to the web version of this article.)

elevated levels of [1-^{13}C]Lac/[1-^{13}C]Pyr ($p = 0.019$) in the CEL, along with higher REC$_{med}$ ($p = 0.047$), elevated k_{PL} ($p = 0.007$) and increased levels of the modified ratio ($p = 0.018$) in the T2L (Fig. 8; Table 2).

4. Discussion

This multi-parametric translational imaging study was designed to investigate active tumor metabolism in patients with HGG using dynamic HP-^{13}C MRI alongside established ^{1}H-based techniques. Voxel-wise regional analysis of anatomic lesions importantly demonstrated alterations in steady-state ^{1}H and dynamic HP-^{13}C metabolism, which highlighted disease relative to NAWM while also revealing hypothesized heterogeneity across contrast-enhancing and non-enhancing subregions. With the ability to probe both glycolytic and oxidative phosphorylation pathways *in vivo*, HP-^{13}C imaging captured the apparent shift toward dysregulated Warburg metabolism (Warburg, 1956; Agnihotri and Zadeh, 2016) in GBM through the excessive and preferential production of [1-^{13}C]lactate over [^{13}C]bicarbonate. This novel mechanism for generating tumor contrast based on the rapid uptake and enzymatic conversion of [1-^{13}C]pyruvate tracer (Autry et al., 2020; Chen et al., 2021) accordingly holds promise for monitoring tumor evolution and treatment. Our preliminary findings on imaging markers characterizing prog/TN GBM in relation to progressive G4A^{IDH+} and benign treatment effects also demonstrated the potential benefit of HP techniques in patient management. Of particular note is that this study surveyed the largest-to-date cohort of patients with progressive glioma who underwent technically-demanding and resource/personnel-intensive HP imaging experiments.

Despite the varied radiological, molecular (Fig. 1) and clinical presentations of individual lesions, prog/TN (Autry et al., 2020; Chen et al., 2021) GBMs universally displayed excess [1-^{13}C]lactate production as a central hallmark of HP imaging. This finding comported with evidence from prior HP studies (Autry et al., 2020; Chen et al., 2021; Zaccagna et al., 2022) regarding the apparent upregulation of aerobic glycolysis in glioma, either measured by AUC [1-^{13}C]lactate or k_{PL}. Furthermore, with the current application of denoising techniques (Kim et al., 2021; Vaziri et al., 2022) enabling voxel-wise analysis, it was possible to show that AUC [1-^{13}C]lactate generally offered improved lesion contrast over k_{PL} for GBM. The most plausible explanation for this phenomenon is that the vascular [1-^{13}C]pyruvate signal emanating from non-metabolically-active substrate dominated kinetic models in common cases of high perfusion (Figs. 6 and 7). As a first attempt at partially accounting for such vascular signal, the modified ratio helped highlight CEL/NEL regions in GBM, but three-compartment kinetic models (Bankson et al., 2015) should also be investigated going forward.

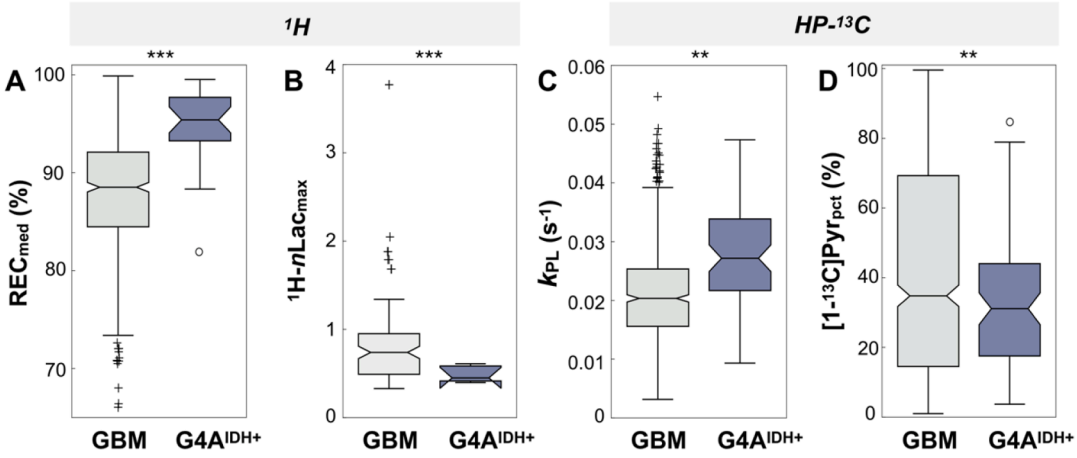

Fig. 5. Features of prog/TN GBM vs G4A^{IDH+}. Statistically significant ^{1}H/HP-^{13}C MRI parameters distinguishing prog/TN GBM versus G4A^{IDH+} in the T2L: REC_{med} (A), ^{1}H-nLac$_{max}$ (B), kinetic rate constant k_{PL} (C) and [1-^{13}C]Pyr$_{pct}$ (D). Mixed effects model significance: $p \leq 0.001$,***; $p \leq 0.01$,**; $p \leq 0.05$,*.

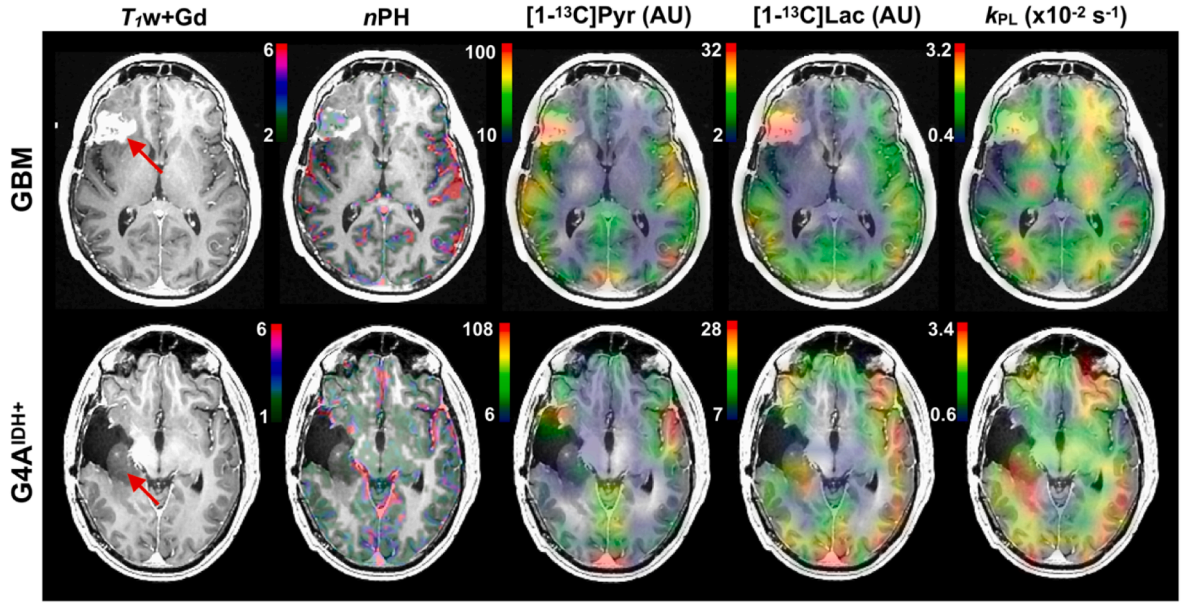

Fig. 6. ^{1}H/HP-^{13}C MRI of progressive GBM vs G4A^{IDH+}. Multi-parametric ^{1}H/HP-^{13}C MRI data from patients with progressive GBM (*top*) and G4A^{IDH+} (*bottom*) are overlaid on T_1-weighted post-Gd images. The GBM lesion demonstrates elevated perfusion from *n*PH and HP [1-^{13}C]Pyr, which likely hindered kinetic modeling when considering the low k_{PL} values despite high HP [1-^{13}C]lactate production. Conversely, the weakly perfused G4A^{IDH+} shows moderate HP [1-^{13}C]Lac production alongside elevated k_{PL}.

Within GBM, excess dynamic production of HP [1-^{13}C]lactate provided an apparent measure of upregulated glycolytic activity in malignant astrocytes (Takahashi, 2021). Whether lactate dehydrogenase-A (LDHA) expression, recently correlated with [1-^{13}C]Lac/[1-^{13}C]Pyr (Zaccagna et al., 2022), or astrocytic proliferation plays an outsized role in [1-^{13}C]lactate accumulation remains an open question, as well as the extent to which vascular metabolism may confound signal attribution (Hu et al., 2022). Compared to dynamic HP [1-^{13}C]lactate production that was visible throughout the brain (Park et al., 2018), steady-state ^{1}H-*n*lactate production was limited to the tumor and associated necrotic regions, with astrocytic MCT transporters regulating intracellular pH in both cases through lactate efflux (Miranda-Goncalves et al., 2013). Acquiring dynamic HP [1-^{13}C]lactate may be of help in quantifying the non-necrotic metabolic pool of lactate related to active tumor, depending on the level and timescale of production. It will be of interest to determine how well steady-state and dynamic measures of lactate correlate with one another, since measuring ^{1}H-lactate in this study was limited by spectroscopic coverage and signal-to-noise ratios.

In addition to improving HP [1-^{13}C]lactate detection, denoising techniques (Kim et al., 2021; Vaziri et al., 2022) importantly helped to demonstrate lower [^{13}C]bicarbonate levels that suggested diminished intralesional mitochondrial oxidative phosphorylation (Saraste, 1999; Shi et al., 2019). Taken together, the excess [1-^{13}C]lactate production, increased [1-^{13}C]lactate-to-[^{13}C]bicarbonate ratios and reduced [^{13}C]bicarbonate-to-[1-^{13}C]pyruvate ratios in lesions supported the capability for HP imaging to capture altered Warburg metabolism *in vivo*, which may benefit the monitoring of tumor evolution amid a backdrop of treatment-related changes on conventional anatomical MRIs (Da Cruz et al., 2011; Thrust et al., 2018).

In the regional analysis of prog/TN GBM, the multi-parametric data enabled extensive characterization of anatomic lesions using both mutual and independent information supplied by ^{1}H and HP-^{13}C modalities. The complementarity of Gd-based and HP [1-^{13}C]pyruvate perfusion with regard to their statistical association and ability to

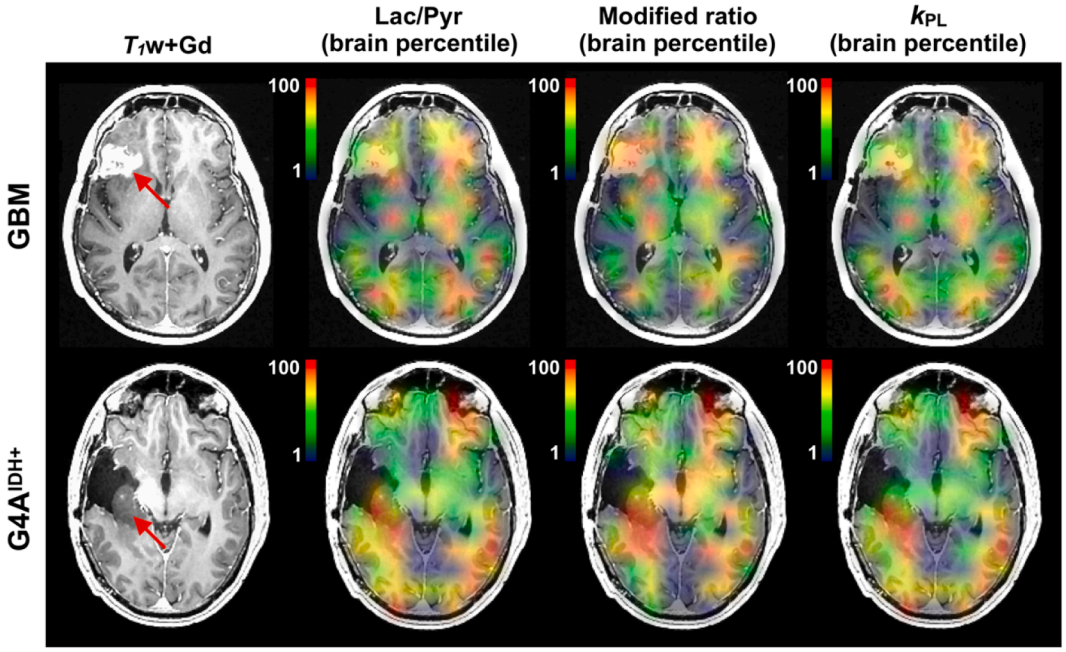

Fig. 7. Modified ratio. Maps of [1-^{13}C]Lac/[1-^{13}C]Pyr, the modified ratio and k_{PL} are presented as percentile values within the brain for patients with progressive GBM (*top*) and G4A^{IDH+} (*bottom*). While [1-^{13}C]Lac/[1-^{13}C]Pyr and k_{PL} maps display similarly low HP contrast in the Gd-enhancing GBM, the modified ratio demonstrates greater lesion contrast by partially accounting for non-metabolically-active vascular substrate. The mostly non-enhancing G4A^{IDH+} lesion is also more broadly highlighted by the modified ratio.

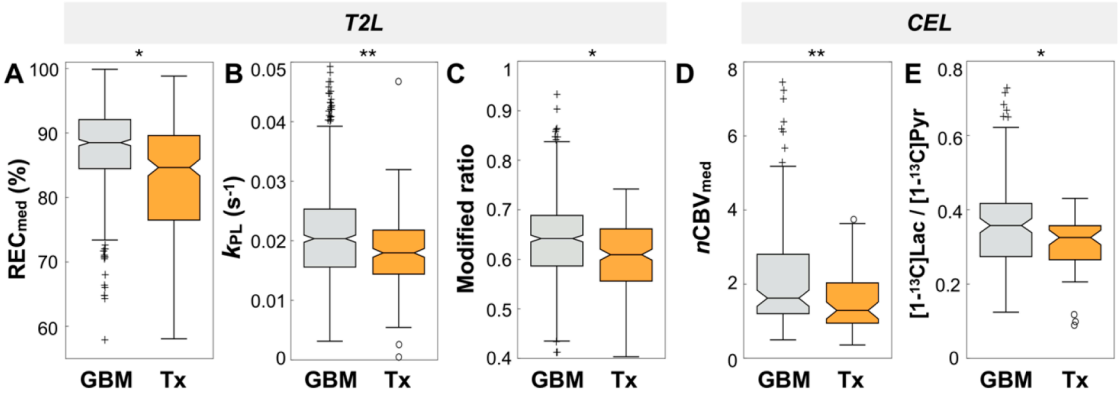

Fig. 8. Features of prog/TN GBM vs treatment effects. Statistically significant ^{1}H/HP-^{13}C MRI parameters distinguishing prog/TN GBM versus treatment-induced effects in patients: REC_{med} (A), kinetic rate constant k_{PL} (B), modified ratio (C), $nCBV_{med}$ (D) and [1-^{13}C]Lac /[1-^{13}C]Pyr (E). Tx, treatment-induced effects. Mixed effects model significance: $p \leq 0.001$,***; $p \leq 0.01$,**; $p \leq 0.05$,*.

identify vascular abnormalities in high-grade disease was a valuable finding, given the importance placed on perfusion metrics for monitoring tumor recurrence (van Dijken et al., 2019; Singh et al., 2016). At the same time, positive associations between DSC perfusion parameters ($nCBV_{med}$, nPH_{med}) and HP [1-^{13}C]pyruvate levels within GBM were likely driven by the highly vascular environment of angiogenic lesions; and, as such, may not adequately reflect subtle differences between these metrics outside of the tumor. This is because unlike chelated Gd contrast agents, [1-^{13}C]pyruvate behaves as an endogenous small molecule with active transport across intact BBB and plasma membrane via MCTs (Grist et al., 2019; Miranda-Goncalves et al., 2013), thus promoting greater mobility and differential localization. These tracer qualities have previously been shown to promote HP [1-^{13}C]pyruvate dissemination in the brain despite normalization of vascular permeability following anti-angiogenic/VEGF therapy with bevacizumab (Autry et al., 2020; Keunen et al., 2011).

Although proton-based measures of perfusion ($nCBV_{med}$, nPH_{med}) consistently isolated CEL from NEL or NAWM, the ^{1}H spectroscopic parameter CNI_{max} was shown to distinguish both Gd-enhancing and non-enhancing lesions from NAWM. This may be because CNI reports on the steady-state metabolism associated with cellular proliferation and neuronal dysfunction (Saraswathy et al., 2009), which represent early markers of active tumor that precede neovascularization from angiogenesis. Correlative analysis further showed that CNI_{max} was positively associated with [1-^{13}C]pyruvate perfusion, [1-^{13}C]lactate production, and the modified ratio, indicating a relative co-localization of abnormal tumor features emanating from the CEL. While elevated *n*ADC similarly characterized the T2L, such diffusion abnormalities are considered less specific to active tumor since they also arise from general alterations in tissue architecture and edema (Kono et al., 2001); conversely, low ADC associated with tumor cellularity may only describe small portion of the lesion.

When comparing prog/TN GBMs against G4A^{IDH+}, the classic GBMs appeared to display much more aggressive imaging characteristics from

the limited data collected. The elevated perfusion in GBM lesions measured by means of [1-^{13}C]Pyr$_{pct}$ probably caused k_{PL} to appear artificially lower than in G4A^{IDH+} for reasons previously mentioned. In addition to presenting higher [1-^{13}C]pyruvate perfusion indicative of BBB-disruption, GBMs displayed lower REC that is typically associated with immature, leaky vasculature resulting from angiogenic processes (Goel et al., 2011). Higher levels of ^{1}H-*n*lactate characterizing GBM may reflect phenotypic differences in metabolic expression compared to G4A^{IDH+} and/or heightened pathologic necrosis, with dynamic [1-^{13}C] lactate production not being a statistically significant factor.

Analysis of tumor versus treatment effects again revealed more aggressive features in the prog/TN lesions. While higher *n*CBV$_{med}$ values in the CEL of prog/TN GBMs were in keeping with traditional perfusion hallmarks of disease, the lower NEL REC in GBMs with treatment effects seemed to indicate worse vascular injuries following radiotherapy. The metabolic lesions of prog/TN GBMs were only highlighted by HP-^{13}C parameters that reported on dynamic [1-^{13}C]lactate production: k_{PL} and the modified ratio in the NEL and the [1-^{13}C]lactate-to-[1-^{13}C]pyruvate ratio in the CEL. These preliminary findings suggest that dynamic HP [1-^{13}C]lactate may hold particular importance for discriminating active tumor and assessing its relative composition in lesions that have undergone treatment.

Interpreting the data in this study presented several technical challenges that extended beyond the limitations in sample sizes among certain cohorts. Perhaps the greatest of these was the disparity in spatial resolution between HP-^{13}C and ^{1}H imaging acquisitions, which caused partial volume effects for the coarser HP data. When interpreting HP-^{13}C data, the general caveats are that experiments deliver non-physiologic doses of exogenous [1-^{13}C]pyruvate tracer and the resulting [1-^{13}C] lactate signal depends at least in part on the endogenous lactate pool (Kennedy et al., 2012; Hurd et al., 2013). Additionally, reporting on individual HP-^{13}C metabolite AUC levels without ratiometric relationships or kinetic modeling is complicated by the spatially-variant sensitivity profiles of multi-channel receiver coils; hence, metabolite maps normalized by hardware sensitivity would be ideal for expressing relative levels, and superior to the percentile maps reported here. Applying such coil correction to both HP-^{13}C and ^{1}H data could improve upon cross-nucleus correlation analysis as well. Depending on the location of the lesion, ^{1}H spectroscopy sometimes failed to provide full coverage due to subcutaneous fat suppression near the skull or low signal regions. Finally, there are several potential confounding factors related to the variation in patient treatment, which ranged from no clinical intervention to standard of care plus multiple adjuvant therapies. This precluded any molecular-based comparisons within prog/TN GBM lesions and analyses between TN versus progressed lesions, but also demonstrated the robustness of certain markers like AUC [1-^{13}C]lactate.

It is also worth noting study limitations related to the interpretation and reliability of the analysis. The clinical assessment of treatment effects and progression by *m*RANO criteria was crucial to defining relevant populations for comparison. While standard 2-month or short-interval follow-up imaging was generally acquired in the absence of histological confirmation, there remained a level of uncertainty from the imaging-based classification of disease status, which carried over to the analysis. A considerable part of the rationale for HP imaging is the potential to determine metabolic status in such cases. Another concern is the smaller patient cohorts that contained subjects who were scanned twice. Although individual imaging timepoints generally demonstrated disparate tumor presentations (see Supplementary Table 1), these exploratory analyses could be affected to some extent by scan weighting.

While HP-^{13}C MRI remains under active development, it holds distinct advantages over existing metabolic imaging techniques which should be emphasized when considering hyperpolarization's complementary role. Because of the multi-order signal enhancement conferred through polarization, HP-^{13}C MRI can uniquely provide a rapid readout of dynamic metabolism within 60 s following tracer delivery. This early metabolic window has recently been exploited in animal (Bogh et al., 2022) and human (Uthayakumar et al., 2022) HP studies as a means of studying the controversial lactate shuttle hypothesis, wherein astrocytes are thought to mediate neuronal energy supply via lactate. Technical experiments from these studies demonstrating that saturation of the [1-^{13}C]lactate resonance reduces [^{13}C]bicarbonate signal indeed support such compartmentalized metabolism.

Compared to longer, steady-state measurements of lactate using ^{1}H 3-D MRSI (~6–7 min), HP data are not confounded by the necrotic lactate pool in gliomas and have the added potential for kinetic modeling. Furthermore, ^{1}H-based lactate-edited acquisitions are more sensitive to magnetic susceptibility effects that give rise to field inhomogeneities causing spectral distortions. Due to the increased volume of excitation required by lactate-edited versus non-edited 3-D ^{1}H MRSI, aliasing of subcutaneous lipid signal can also contaminate large swathes of lactate data based on its shear amplitude (Park et al., 2011).

It is also worth highlighting the comparative advantages of HP-^{13}C imaging relative to deuterium metabolic imaging (DMI), which can analogously probe Warburg alterations in glioma using orally-administered ^{2}H-labeled glucose (De Feyter et al., 2018). Despite a variety of trade-offs between the two MR-based techniques, a side-by-side comparison study at clinical field strengths demonstrated that HP-^{13}C MRSI offered greater signal-to-noise, along with improved spatial, spectral and temporal resolution, while being more robust to field inhomogeneity (Kaggie et al., 2022). Both techniques were considered complementary in the study from the perspective that HP-^{13}C was weighted toward early reductive metabolism immediately following [1-^{13}C]pyruvate delivery whereas DMI captured the shift toward oxidative metabolism during the steady state, approximately 57 min. post [6,6′-^{2}H$_2$]glucose consumption. With the capacity to measure early substrate-mediated metabolic changes on the order of seconds, HP techniques fulfill a distinct imaging niche that deserves further investigation alongside DMI.

This multi-parametric HP-^{13}C/^{1}H MRI study has demonstrated the real-time acquisition of dynamic Warburg-related metabolism in patients with molecularly-diverse progressive GBM and characterized associated tumor heterogeneity in a novel manner with the combination of dynamic and steady-state imaging experiments. Because evaluating disease status in treated GBM remains a central diagnostic dilemma within neuro-oncology, the value of HP-^{13}C MRI lies in its potential to detect Warburg-related metabolic changes that may predict tumor progression and therapeutic response in advance. The sensitivity for such detection is poised to improve markedly with the near-term implementation of 7 Tesla polarizers and medium-term reduction in the dissolution-to-injection time over which ^{13}C magnetization decays exponentially. Ongoing development and dissemination of HP methods are anticipated to enhance the generalizability and translation of the advanced metabolic imaging reported here.

CRediT authorship contribution statement

Adam W. Autry: Conceptualization, Methodology, Investigation, Writing – original draft, Formal analysis, Visualization, Data curation. **Sana Vaziri:** Methodology, Investigation, Data curation, Validation, Writing – review & editing. **Marisa LaFontaine:** Investigation, Data curation, Writing – review & editing. **Jeremy W. Gordon:** Methodology, Validation, Writing – review & editing. **Hsin-Yu Chen:** Methodology, Validation, Writing – review & editing. **Yaewon Kim:** Methodology, Validation, Writing – review & editing. **Javier E. Villanueva-Meyer:** Conceptualization, Writing – review & editing. **Annette Molinaro:** Formal analysis, Writing – review & editing. **Jennifer L. Clarke:** Conceptualization, Funding acquisition, Writing – review & editing. **Nancy Ann Oberheim Bush:** Conceptualization, Funding acquisition, Writing – review & editing. **Duan Xu:** Funding acquisition, Writing – review & editing. **Janine M. Lupo:** Conceptualization, Writing – review & editing. **Peder E.Z. Larson:** Methodology, Conceptualization, Writing – review & editing. **Daniel B. Vigneron:** Conceptualization, Resources,

Funding acquisition, Writing – review & editing. **Susan M. Chang:** Conceptualization, Funding acquisition, Writing – review & editing. **Yan Li:** Conceptualization, Funding acquisition, Supervision, Project administration, Writing – review & editing.

Declaration of Competing Interest

The authors declare that they have no known competing financial interests or personal relationships that could have appeared to influence the work reported in this paper.

Data availability

Data will be made available on request.

Acknowledgements

We would like to acknowledge the patients and their families for their participation in this study. We are also grateful for the HP research support provided by the Surbeck Lab for Advanced Imaging. This work was supported by National Institutes of Health grants P50 CA097257, P01 CA118816, P41 EB013598, R01 CA262630, T32 CA151022 (AA, SV); and the Glioblastoma Precision Medicine Program.

Appendix A. Supplementary material

Supplementary data to this article can be found online at https://doi.org/10.1016/j.nicl.2023.103501.

References

Agnihotri, S., Zadeh, G., 2016. Metabolic reprogramming in glioblastoma: the influence of cancer metabolism on epigenetics and unanswered questions. Neuro-Oncol. 18 (2), 160–172.

Ardenkjaer-Larsen, J.H., Fridlund, B., Gram, A., Hansson, G., Hansson, L., Lerche, M.H., et al., 2003. Increase in signal-to-noise ratio of >10,000 times in liquid-state NMR. Proc. Natl. Acad. Sci. 100, 10158–10163.

Autry, A.W., Gordon, J.W., Chen, H.-Y., LaFontaine, M., Bok, R., Van Criekinge, M., Slater, J.B., Carvajal, L., Villanueva-Meyer, J.E., Chang, S.M., Clarke, J.L., Lupo, J. M., Xu, D., Larson, P.E.Z., Vigneron, D.B., Li, Y., 2020. Characterization of serial hyperpolarized-^{13}C metabolic imaging in patients with glioma. NeuroImage: Clin. 27.

Autry, A.W., Park, I., Kline, C., Chen, H.-Y., Gordon, J.W., Raber, S., Hoffman, C., Kim, Y., Okamoto, K., Vigneron, D.B., Lupo, J.M., Prados, M., Li, Y., Xu, D., Mueller, S., 2021. Pilot study of hyperpolarized-^{13}C metabolic imaging in pediatric patients with diffuse intrinsic pontine glioma and other CNS Cancers. Am. J. Neuroradiol. 42 (1), 178–184.

Bankson, J.A., Walker, C.M., Ramirez, M.S., Stefan, W., Fuentes, D., Merritt, M.E., Lee, J., Sandulache, V.C., Chen, Y., Phan, L., Chou, P.-C., Rao, A., Yeung, S.-C., Lee, M.-H., Schellingerhout, D., Conrad, C.A., Malloy, C., Sherry, A.D., Lai, S.Y., Hazle, J.D., 2015. Kinetic modeling and constrained reconstruction of hyperpolarized [1-13C] pyruvate offers improved metabolic imaging of tumors. Cancer Res. 75 (22), 4708–4717.

Basser, P.J., Pierpaoli, C., 1996. Microstructural and physiological features of tissues elucidated by quantitative-diffusion-tensor MRI. J. Magn. Reson. 111, 209–219.

Bogh, N., Grist, J.T., Rasmussen, C.W., Bertelsen, L.B., Hansen, E.S.S., Blincher, J.U., et al., 2022. Lactate saturation limits bicarbonate detection in hyperpolarized ^{13}C-pyruvate MRI of the brain. Magn. Reson. Med. 88 (3), 1170–1179.

Chen, J., Patel, T.R., Pinho, M.C., Choi, C., Harrison, C.E., Baxter, J.D., et al., 2021. Preoperative imaging of glioblastoma patients using hyperpolarized 13C-pyruvate: Potential role in clinical decision making. Neuro-Oncol. Adv. 3 (1), vdab092.

Crane, J., Olson, M.P., Nelson, S.J., 2013. SIVIC: Open-source Standards-based software for DICOM spectroscopy workflows. Int. J. Biomed. Imaging 2013, 169526.

Da Cruz, L.C.H., Rodriguez, I., Domingues, R.C., Gasparetto, E.L., Sorensen, A.G., 2011. Pseudoprogression and pseudoresponse: imaging challenges in the assessment of posttreatment glioma. Am. J. Neuroradiol. 32 (11), 1978–1985.

De Feyter, H.M., Behar, K.L., Corbin, Z.A., Fulbright, R.K., Brown, P.B., McIntyre, S., Nixon, T.W., Rothman, D.L., de Graaf, R.A., 2018. Deuterium metabolic imaging (DMI) for MRI-based 3D mapping of metabolism in vivo. Sci. Adv. 4 (8).

Ellingson, B.M., Wen, P.Y., Cloughesy, T.F., 2017. Modified criteria for radiographic response assessment in glioblastoma clinical trials. Neurotherapeutics 14 (2), 307–320.

Goel, S., Duda, D.G., Xu, L., Munn, L.L., Boucher, Y., Fukumura, D., Jain, R.K., 2011. Normalization of the vasculature for treatment of cancer and other diseases. Physiol. Rev. 91 (3), 1071–1121.

Gordon, J.W., Chen, H.Y., Autry, A.W., Park, I., Van Criekinge, M., Mammoli, D., et al., 2019. Translation of carbon-13 EPI for hyperpolarized MR molecular imaging of prostate and brain cancer patients. Magn. Reson. Med. 81, 2702–2709.

Grist, J.T., McLean, M.A., Riemer, F., Schulte, R.F., Deen, S.S., Zaccagna, F., Woitek, R., Daniels, C.J., Kaggie, J.D., Matys, T., Patterson, I., Slough, R., Gill, A.B., Chhabra, A., Eichenberger, R., Laurent, M.-C., Comment, A., Gillard, J.H., Coles, A.J., Tyler, D.J., Wilkinson, I., Basu, B., Lomas, D.J., Graves, M.J., Brindle, K.M., Gallagher, F.A., 2019. Quantifying normal human brain metabolism using hyperpolarized [1-13C] pyruvate and magnetic resonance imaging. Neuroimage 189, 171–179.

Hu, J.Y., Kim, Y., Autry, A.W., Frost, M.M., Bok, R.A., Villanueva-Meyer, J.E., Xu, D., Li, Y., Larson, P.E.Z., Vigneron, D.B., Gordon, J.W., 2022. Kinetic analysis of multi-resolution hyperpolarized-^{13}C human brain MRI to study cerebral metabolism. Magn. Reson. Med. 88 (5), 2190–2197.

Hurd, R.E., Spielman, D., Josan, S., Yen, Y.-F., Pfefferbaum, A., Mayer, D., 2013. Exchange-linked dissolution agents in dissolution-DNP (13)C metabolic imaging. Magn. Reson. Med. 70 (4), 936–942.

Jenkinson, M., Smith, S.M., 2001. A global optimisation method for robust affine registration of brain images. Med. Image Anal. 5, 143–156.

Kaggie, J.D., Khan, A.S., Matys, T., Schulte, R.F., Locke, M.J., Grimmer, A., et al., 2022. Deuterium metabolic imaging and hyperpolarized 13C-MRI of the normal human brain at clinical field strength reveals differential cerebral metabolism. Neuroimage 257, 119284.

Kennedy, B.W.C., Kettunen, M.I., Hu, D.E., Brindle, K.M., 2012. Probing lactate dehydrogenase activity in tumors by measuring hydrogen/deuterium exchange in hyperpolarized l-[1-(13)C, U-(2)H]lactate. J. Am. Chem. Soc. 134 (10), 4969–4977.

Keunen, O., Johansson, M., Oudin, A., Sanzey, M., Rahim, S.A.A., Fack, F., et al., 2011. Anti-VEGF treatment reduces blood supply and increases tumor cell invasion in glioblastoma. Proc. Natl. Acad. Sci. 108 (9), 3749–3754.

Kim, Y., Chen, H.Y., Autry, A.W., Villanueva-Meyer, J., Chang, S.M., Li, Y., et al., 2021. Denoising of hyperpolarized-^{13}C MR images of the human brain using patch-based higher-order singular value decomposition. Magn. Reson. Med. 86, 2497–2511.

Kono, K., Inoue, Y., Nakayama, K., Shakudo, M., Morina, M., Ohata, K., et al., 2001. The role of diffusion-weighted imaging in patients with brain tumors. Am. J. Neuroradiol. 22 (6), 1081–1088.

Larson, P.E.Z., Chen, H.-Y., Gordon, J.W., Korn, N., Maidens, J., Arcak, M., Tang, S., Criekinge, M., Carvajal, L., Mammoli, D., Bok, R., Aggarwal, R., Ferrone, M., Slater, J.B., Nelson, S.J., Kurhanewicz, J., Vigneron, D.B., 2018. Investigation of analysis methods for hyperpolarized ^{13}C-pyruvate metabolic MRI in prostate cancer patients. NMR Biomed. 31 (11), e3997.

Lee, C.Y., Soliman, H., Geraghty, B.J., Chen, A.P., Connelly, K.A., Endre, R., Perks, W.J., Heyn, C., Black, S.E., Cunningham, C.H., 2020. Lactate topography of the human brain using hyperpolarized ^{13}C-MRI. Neuroimage 204.

Lee, C.Y., Soliman, H., Bragagnolo, N.D., Sahgal, A., Geraghty, B.J., Chen, A.P., Endre, R., Perks, W.J., Detsky, J.S., Leung, E., Chan, M., Heyn, C., Cunningham, C. H., 2021. Predicting response to radiotherapy of intracranial metastases with hyperpolarized-^{13}C MRI. J. Neuro-Oncol. 152 (3), 551–557.

Louis, D.N., Perry, A., Wesseling, P., Brat, D.J., Cree, I.A., Figarella-Branger, D., Hawkins, C., Ng, H.K., Pfister, S.M., Reifenberger, G., Soffietti, R., von Deimling, A., Ellison, D.W., 2021. The 2021 WHO classification of tumors of the central nervous system: a summary. Neuro-Oncol. 23 (8), 1231–1251.

Lunt, Y.L., Vander Heiden, M.G., 2011. Aerobic glycolysis: meeting the metabolic requirements of cell proliferation. Annu. Rev. Cell Dev. Biol. 27, 441–464.

Lupo, J.M., Cha, S., Chang, S.M., Nelson, S.J., 2007. Analysis of metabolic indices in regions of abnormal perfusion in patients with high-grade glioma. Am. J. Neuroradiol. 28 (8), 1455–1461.

McKnight, T.R., Noworolski, S.M., Vigneron, D.B., Nelson, S.J., 2001. An automated technique for the quantitative assessment of 3D-MRSI data from patients with glioma. J. Magn. Reson. Imaging 13, 167–177.

Menze, B.H., Jakab, A., Bauer, S., Kalpathy-Cramer, J., Farahani, K., Kirby, J., Burren, Y., Porz, N., Slotboom, J., Wiest, R., Lanczi, L., Gerstner, E., Weber, M.-A., Arbel, T., Avants, B.B., Ayache, N., Buendia, P., Collins, D.L., Cordier, N., Corso, J.J., Criminisi, A., Das, T., Delingette, H., Demiralp, C., Durst, C.R., Dojat, M., Doyle, S., Festa, J., Forbes, F., Geremia, E., Glocker, B., Golland, P., Guo, X., Hamamci, A., Iftekharuddin, K.M., Jena, R., John, N.M., Konukoglu, E., Lashkari, D., Mariz, J.A., Meier, R., Pereira, S., Precup, D., Price, S.J., Raviv, T.R., Reza, S.M.S., Ryan, M., Sarikaya, D., Schwartz, L., Shin, H.-C., Shotton, J., Silva, C.A., Sousa, N., Subbanna, N.K., Szekely, G., Taylor, T.J., Thomas, O.M., Tustison, N.J., Unal, G., Vasseur, F., Wintermark, M., Ye, D.H., Zhao, L., Zhao, B., Zikic, D., Prastawa, M., Reyes, M., Van Leemput, K., 2015. The multimodal brain tumor image segmentation benchmark (BRATS). IEEE Trans. Med. Imaging 34 (10), 1993–2024.

Miloushev, V.Z., Granlund, K.L., Boltyanskiy, R., Lyashchenko, S.K., DeAngelis, L.M., Mellinghoff, I.K., Brennan, C.W., Tabar, V., Yang, T.J., Holodny, A.I., Sosa, R.E., Guo, Y.W., Chen, A.P., Tropp, J., Robb, F., Keshari, K.R., 2018. Metabolic imaging of the human brain with hyperpolarized ^{13}C-pyruvate demonstrates ^{13}C-lactate production in brain tumor patients. Cancer Res. 78 (14), 3755–3760.

Miranda-Gonçalves, V., Honavar, M., Pinheiro, C., Martinho, O., Pires, M.M., Pinheiro, C., Cordeiro, M., Bebiano, G., Costa, P., Palmeirim, I., Reis, R.M., Baltazar, F., 2013. Monocarboxylate transporters (MCTs) in gliomas: expression and exploitation as therapeutic targets. Neuro-Oncol. 15 (2), 172–188.

Nash J.C. The Choleski decomposition. In: Compact numerical methods for computers: linear algebra and function minimization, 2nd ed. New York: Adam Hilger; 1990. p. 84-93.

Nelson, S.J., 2001. Analysis of volume MRI and MR spectroscopic imaging data for the evaluation of patients with brain tumors. Mag. Reson. Med. 46 (2), 228–239.

Park, I., Chen, A.P., Zierhut, M.L., Ozturk-Isik, E., Vigneron, D.B., Nelson, S.J., 2011. Implementation of 3T lactate-edited 3D ^{1}H MR spectroscopic imaging with flyback echo-planar readout for gliomas patients. Ann. Biomed. Eng. 39 (1), 193–204.

Park, I., Larson, P.E.Z., Gordon, J.W., Carvajal, L., Chen, H.Y., Bok, R., et al., 2018. Development of methods and feasibility of using hyperpolarized carbon-13 imaging data for evaluating brain metabolism in patient studies. Magn. Reson. Med. 80, 864–873.

Rolls, E.T., Huang, C.-C., Lin, C.-P., Feng, J., Joliot, M., 2020. Automated anatomical labelling atlas 3. Neuroimage 206.

Saraste, M., 1999. Oxidative phosphorylation at the fin de siècle. Science 283 (5407), 1488–1493.

Saraswathy, S., Crawford, F.W., Lamborn, K.R., Pirzkall, A., Chang, S., Cha, S., Nelson, S. J., 2009. Evaluation of MR markers that predict survival in patients with newly diagnosed GBM prior to adjuvant therapy. J. Neuro-Oncol. 91 (1), 69–81.

Shi, Y., Lim, S.K., Liang, Q., Iyer, S.V., Wang, H.-Y., Wang, Z., Xie, X., Sun, D., Chen, Y.-J., Tabar, V., Gutin, P., Williams, N., De Brabander, J.K., Parada, L.F., 2019. Gboxin is an oxidative phosphorylation inhibitor that targets glioblastoma. Nature 567 (7748), 341–346.

Singh, R., Kesavabhotla, K., Kishore, S.A., Zhou, Z., Tsiouris, A.J., Filippi, C.G., Boockvar, J.A., Kovanlikaya, I., 2016. Dynamic susceptibility contrast-enhanced MR perfusion imaging in assessing recurrent glioblastoma response to superselective intra-arterial bevacizumab therapy. Am. J. Neuroradiol. 37 (10), 1838–1843.

Takahashi, S., 2021. Neuroprotective function of high glycolytic activity in astrocytes: common roles in stroke and neurodegenerative diseases. Int. J. Mol. Sci. 22 (12), 6568.

Thrust, S., van den Bent, M., Smits, M., 2018. Pseudoprogression of brain tumors. J. Magn. Reson. Imaging 48 (3), 571–589.

Uthayakumar B., Bragagnolo N., Soliman H., Chen A.P., Endre R., Perks W.J., et al. Evidence of lactate shuttling in the human brain with hyperpolarized ^{13}C-MRI. *Proc. Int. Soc. Magn. Reson. Med.* 2022;Abstract#1067.

van Dijken, B.R.J., van Laar, P.J., Smits, M., 2019. Perfusion MRI in treatment evaluation of glioblastomas: clinical relevance of current and future techniques. J. Magn. Reson. Imaging 49 (1), 11–12.

Vaziri, S., Autry, A.W., Lafontaine, M., Kim, Y., Gordon, J.W., Chen, H.-Y., Hu, J.Y., Lupo, J.M., Chang, S.M., Clarke, J.L., Villanueva-Meyer, J.E., Bush, N.A.O., Xu, D., Larson, P.E.Z., Vigneron, D.B., Li, Y., 2022. Assessment of higher-order singular value decomposition denoising methods on dynamic hyperpolarized [1-13C] pyruvate MRI data from patients with glioma. NeuroImage: Clin. 36, 103155.

Warburg, O., 1956. On respiratory impairment in cancer cells. Science 124 (3215), 269–270.

Zaccagna, F., McLean, M.A., Grist, J.T., Kaggie, J., Mair, R., Riemer, F., Woitek, R., Gill, A.B., Deen, S., Daniels, C.J., Ursprung, S., Schulte, R.F., Allinson, K., Chhabra, A., Laurent, M.-C., Locke, M., Frary, A., Hilborne, S., Patterson, I., Carmo, B.D., Slough, R., Wilkinson, I., Basu, B., Wason, J., Gillard, J.H., Matys, T., Watts, C., Price, S.J., Santarius, T., Graves, M.J., Jefferies, S., Brindle, K.M., Gallagher, F.A., 2022. Imaging glioblastoma metabolism by using hyperpolarized [1-13C]pyruvate demonstrates heterogeneity in lactate labeling: a proof of principle study. Radiol. Imaging Cancer 4 (4), e210076.

Zhang, Y., Brady, M., Smith, S., 2001. Segmentation of brain MR images through a hidden random field model and the expectation maximization algorithm. IEEE Trans. Med. Imaging 20, 45–57.

Zhu, Z., Zhu, X., Ohliger, M., Tang, S., Cao, P., Carvajal, L., et al., 2019. Coil combination methods for multi-channel hyperpolarized-^{13}C imaging data from human studies. J. Magn. Reson. 301, 73–139.